Petroleum Science 23 (2026) 178–189

Contents lists available at ScienceDirect

Petroleum Science

journal homepage: www.keaipublishing.com/en/journals/petroleum-science

Original Paper

Characterization of multiple fractured layers using a rock-physics-based shear wave splitting analysis: Application to four-component VSP

Yi-Bo Chai [a,b], Feng Zhang [a,*], Tao Xu [b], Zhen Zou [c], Xiang-Yang Li [a,c]

[a] College of Geophysics, China University of Petroleum (Beijing), Beijing, 102249, China
[b] College of Science, China University of Petroleum (Beijing), Beijing, 102249, China
[c] Bureau of Geophysical Prospecting INC., CNPC, Zhuozhou, 072750, Hebei, China

ARTICLE INFO

Article history:
Received 16 February 2025
Received in revised form
18 August 2025
Accepted 23 September 2025
Available online 29 September 2025

Edited by Meng-Jiao Zhou

Keywords:
Fracture characterization
Shear wave splitting
S-wave source VSP
Inversion

ABSTRACT

Shear wave splitting (SWS) analysis has been widely employed for fracture characterization in both global seismology and seismic exploration. Two key SWS attributes—fast shear wave polarization and the time delay between fast and slow shear waves—can be inverted from four-component seismic data (two horizontal sources and two horizontal receivers). These SWS attributes enable the characterization of subsurface fracture parameters, such as fracture strike and density. In this study, a nine-component vertical seismic profile (VSP) survey was acquired in the Sanhu Depression of the eastern Qaidam Basin, northwestern China. Preliminary analysis of the shear-wave source VSP data reveals two distinct SWS signatures at different depths, corresponding to two separate fractured layers. However, characterizing multiple fractured layers presents significant challenges, as the SWS attributes of deeper fractured layers are strongly influenced by those of overlying fractured formations. Existing approaches for predicting multi-layer fracture parameters are predominantly data-driven and are largely limited to qualitative analysis. To address these challenges, we propose a robust, rock-physics-model-guided method that enables the quantitative estimation of both the fracture strike and fracture density in multiple fractured layers. First, the parameters of the shallow fractured layer are directly estimated from the SWS attributes. Then, synthetic VSP records of the deeper fractured layer are modeled by incorporating Hudson's theory and the reflectivity method. The fracture parameters of the deep fractured layer are inverted by minimizing the difference between the SWS attributes of synthetic records and those of the actual seismic data. A hierarchical search strategy (coarse-scale + refined-scale) is employed to accelerate convergence toward the optimal solution. This investigation provides a practical tool for quantitative characterization of subsurface formations with multiple fractured layers.

1. Introduction

Shear waves propagating through a fractured layer can split into a fast shear wave and a slow shear wave. The polarization of the fast shear wave is aligned with the fracture strike, whereas the polarization of the slow shear wave is oriented perpendicular to the fracture strike. Shear wave splitting (SWS) analysis can be performed using the four-component VSP (vertical seismic profile) data, four-component surface seismic data, and the PS converted waves from three-component surface seismic data, and has been extensively used to characterize fractured formations (e.g., Crampin, 1984; Garotta and Granger, 1988; Mueller, 1991; Yardley and Crampin, 1991; Corrigan et al., 1996; Li, 1998; Guo, 2008; Li, 2011; Ding, 2015; Liu, 2019; Li, 2020; Li et al., 2022; Li, 2024).

Various SWS analysis methods have been investigated (Alford, 1986; Thomsen, 1988; Silver et al., 1991; Bale et al., 2009; Xiao et al., 2013; Prajapati, 2015; Donati et al., 2016; Gholami et al., 2016; Wang, 2020; Gong et al., 2022). Maultzsch (2003) compared different methods and demonstrated that the Linear Transform Technique (LTT) developed by Li and Crampin (1993) is

* Corresponding author.
E-mail address: zhangfeng@cup.edu.cn (F. Zhang).
Peer review under the responsibility of China University of Petroleum (Beijing).

https://doi.org/10.1016/j.petsci.2025.09.038

an efficient and flexible method for analyzing the SWS attributes of four-component seismic shear wave data. However, obtaining the fracture parameters of deep fractured layers using SWS attributes remains challenging, because the SWS attributes of shallow fractured formations can significantly affect those of the deep layers. Thomsen et al. (1999) proposed a layer-stripping SWS analysis method for characterizing multiple fractured layers. However, since this method does not incorporate rock physics to establish a quantitative relationship between fracture parameters and seismic attributes (Wu, 2023, 2024), it is limited to qualitatively characterizing fracture development.

In this paper, we present a rock-physics-based method to determine fracture parameters for multiple fractured layers. This method is applied to the S-wave-source four-component VSP obtained from the eastern Qaidam Basin. First, the VSP data are preprocessed to obtain a high-quality downgoing wavefield, which is then used for SWS analysis. The SWS analysis results reveal two distinct characteristics from shallow to deep layers, indicating the presence of two fractured layers. Next, the thicknesses of these fractured layers are further determined based on the geological background model established from logging data. The shallow fracture parameters can be directly determined from the SWS attributes. However, due to the significant influence of the shallow fractured layer on the SWS attributes of the deep layer, obtaining the deep fracture parameters presents challenges. To address this issue, Hudson's theory and the reflectivity method are used to model synthetic VSP records of the deep fractured layer. The LTT method is then applied to perform SWS analysis on the synthetic seismic records. Finally, the deep fracture parameters are inverted by minimizing the difference between the SWS attributes of the synthetic records and the actual seismic data.

2. Geological background and processing of four-component VSP data

The Quaternary formations in the Sanhu Depression consist of a series of sand-shale interbeds and contain significant biogas resources (Heggland, 1997; Kang et al., 2009; Huang, 2010; Sun, 2011; Wang et al., 2019). A nine-component zero-offset VSP survey was acquired in this area to investigate the subsurface structures (the location of the VSP well is indicated by the red pentagram in Fig. 1). The acquisition geometry is shown in Fig. 2(a). The source geometry is defined in the Cartesian coordinate system *X*, *Y*, and *Z*, while the geophone geometry is defined in the Cartesian coordinate system *x*, *y*, and *z*. The *X*- and *Y*-axes align with the vibration directions of the two horizontal force sources, respectively. The distance from the sources to the well is 33.31 m. The geophones are positioned at depths ranging from 10 m to 1600 m. The seismic records obtained from depths between 10 m and 200 m are significantly contaminated by noise due to the influence of shallow geological structures and surface noise. Fig. 2(b) shows the data matrix for the nine-component recording geometry, with the S-wave four-component records used to investigate the SWS attributes (the hatched area in Fig. 2(b)). Fig. 3 shows the nine-component seismic records acquired by the VSP acquisition geometry (displayed with automatic gain control, AGC). The seismic arrivals exhibit discontinuities, and amplitude anomalies are observed in certain traces. Preprocessing is required before performing SWS analysis.

The raw VSP shot gathers are first processed by removing duplicate traces and correcting amplitude anomalies (Fu, 2025). Then, multi-component amplitude compensation is applied to correct amplitude attenuation caused by geometric spreading, inter-component energy disparity, and other factors, ensuring that the energy levels of all components are consistent. Since the horizontal geophones are placed in boreholes and their orientations are inconsistent, the recorded arrivals exhibit discontinuities. To address this, geophone orientations are corrected using the polarization analysis method (Greenhalgh, 1995). The excited P-wave, which does not exhibit splitting, is used as the reference. The amplitude of the P-wave received by the horizontal geophones with an arbitrary rotation angle φ can be expressed as

$$A_{\mathrm{p}} = \sum_{i}^{n} [x(t_i)\cos\varphi + y(t_i)\sin\varphi]^2, \tag{1}$$

where n is the length of the time window, t is sampling time, and i is the sample index. $x(t_i)$ and $y(t_i)$ denote the seismic records received by the two horizontal components at time t_i. Letting $\frac{\partial A_{\mathrm{p}}}{\partial \varphi} = 0$, the rotation angle can be solved as

$$\varphi = \frac{1}{2}\arctan\frac{2\sum_{i}^{N} x(t_i)y(t_i)}{\sum_{i}^{N}\left[x^2(t_i) - y^2(t_i)\right]}. \tag{2}$$

Fig. 4 shows the calculated rotation angle φ of the geophones varied with depth. The seismic records become significantly more continuous after orientation correction (Fig. 5(a) and (b)). Additionally, the anomalies observed by geophones No. 80 to No. 180 (500–1600 m) are also effectively removed. The upgoing and downgoing wavefields are then separated using F-K (frequency-wavenumber) filtering, as shown in Fig. 5(c) and (d). The downgoing wavefield exhibits higher resolution and signal-to-noise ratio, making it suitable for subsequent SWS analysis.

3. SWS analysis using the Linear Transform Technique

SWS attributes reflect the characteristics of fractures, making SWS analysis a common method for estimating fracture parameters. The original four-component data, denoted as *Xx*, *Xy*, *Yx*, and *Yy*, as illustrated in Fig. 2, cannot be directly used for SWS analysis and must first be transformed into the fast and slow shear-wave coordinate system. The relationship among source coordinate (*X*, *Y*), receiver coordinate (*x*, *y*), and natural fracture coordinate (S1, S2) is illustrated in Fig. 6. S1 is along the fracture strike, while S2 is perpendicular to the fracture strike. The LTT proposed by Li and Crampin (1993) enables the conversion of the four-component shear-wave data from complex motions into linear motions. α is the angle between *X* and *x*, and θ is the angle between S1 and *x*. α and θ can be estimated during the separation of fast and slow shear waves.

The four-component data matrix, acquired using two horizontal sources (vibrating along the *X* and *Y*) and two orthogonal receiver components (recorded along *x* and *y*), can be expressed as

$$\mathbf{D}(t) = \begin{bmatrix} Xx(t) & Xy(t) \\ Yx(t) & Yy(t) \end{bmatrix}, \tag{3}$$

where t denotes the sampling time. The four-component records can be further written:

$$\begin{aligned} Xx(t) &= \mathrm{qS1}(t)\cos\theta\cos(\alpha+\theta) + \mathrm{qS2}(t)\sin\theta\sin(\alpha+\theta), \\ Xy(t) &= \mathrm{qS1}(t)\sin\theta\cos(\alpha+\theta) - \mathrm{qS2}(t)\cos\theta\sin(\alpha+\theta), \\ Yx(t) &= \mathrm{qS1}(t)\cos\theta\sin(\alpha+\theta) - \mathrm{qS2}(t)\sin\theta\cos(\alpha+\theta), \\ Yy(t) &= \mathrm{qS1}(t)\sin\theta\sin(\alpha+\theta) + \mathrm{qS2}(t)\cos\theta\cos(\alpha+\theta), \end{aligned} \tag{4}$$

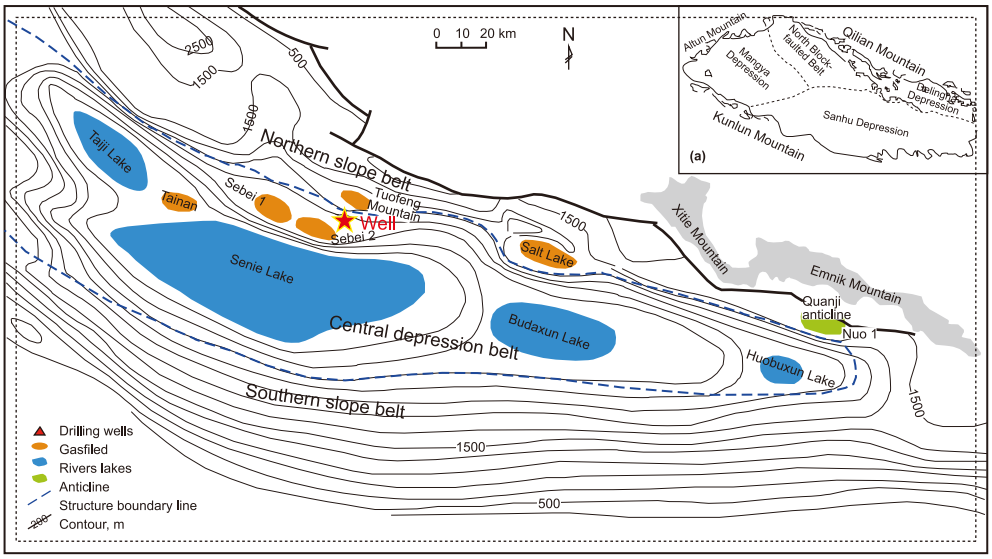

Fig. 1. Map of the Sanhu area in the Qaidam Basin, China, showing the location of the VSP well.

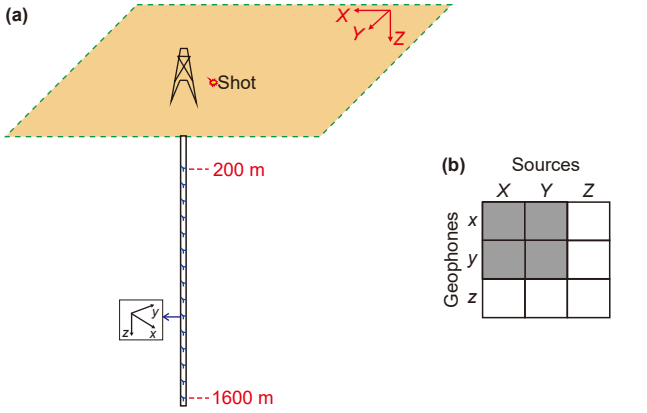

Fig. 2. **(a)** The acquisition geometry of the nine-component VSP. **(b)** Nine-component seismic excited by three orthogonal sources (*X*, *Y*, *Z*) and received by three orthogonal receivers (*x*, *y*, *z*). The hatched area represents two-by-two shear-wave recordings (two horizontal sources and two horizontal receivers).

where qS1 is the seismic records of the fast shear wave polarized along the S1, qS2 is the seismic records of the slow shear wave polarized along S2. α and θ need to be determined for the separation of qS1 and qS2.

Li and Crampin (1993) applied a set of linear operations to the four-component data (*Xx*, *Xy*, *Yx*, and *Yy*), yielding a new set of transformed components (ξ, η, ζ, and χ):

$$\begin{aligned}\xi(t) &= Xx(t) - Yy(t) = [\mathrm{qS1}(t) - \mathrm{qS2}(t)]\cos(\alpha + 2\theta),\\ \eta(t) &= Xy(t) + Yx(t) = [[\mathrm{qS1}(t) - \mathrm{qS2}(t)]]\sin(\alpha + 2\theta),\\ \zeta(t) &= Xx(t) + Yy(t) = [[\mathrm{qS1}(t) + \mathrm{qS2}(t)]]\cos\alpha,\\ \chi(t) &= Yx(t) - Xy(t) = [[\mathrm{qS1}(t) + \mathrm{qS2}(t)]]\sin\alpha,\end{aligned} \tag{5}$$

Consequently, the angles $\alpha+2\theta$ and α can be estimated through linear regression as follows:

$$\alpha + 2\theta = \frac{1}{2}\tan^{-1}\left[\frac{2\sum_\tau \xi(t+\tau)\eta(t+\tau)}{\sum_\tau\left[\xi^2(t+\tau) - \eta^2(t+\tau)\right]}\right], \tag{6}$$

$$\alpha = \frac{1}{2}\tan^{-1}\left[\frac{\sum_\tau \zeta(t+\tau)\chi(t+\tau)}{\sum_\tau\left[\zeta^2(t+\tau) - \chi^2(t+\tau)\right]}\right], \tag{7}$$

where τ is the scanning time window.

Then the fast and slow shear waves are separated as

$$\begin{aligned}\mathrm{qS1}(t) = \frac{1}{2}\Big[&\xi(t)\cos(\alpha) + \eta(t)\sin(\alpha),\\ &+(\zeta(t)\cos(\alpha + 2\theta) + \chi(t)\sin(\alpha + 2\theta))\Big],\\ \mathrm{qS2}(t) = \frac{1}{2}\Big[&\xi(t)\cos(\alpha) + \eta(t)\sin(\alpha)\\ &-(\zeta(t)\cos(\alpha + 2\theta) + \chi(t)\sin(\alpha + 2\theta))\Big].\end{aligned} \tag{8}$$

The time delay between the fast and slow shear waves is expressed using the covariance matrix method as

$$\mathbf{D}(\Delta t) = \begin{bmatrix} \sum_{i=1}^{N}(\mathrm{qS1}(t) - \overline{\mathrm{qS1}(t)})^2 & \sum_{i=1}^{N}(\mathrm{qS1}(t) - \overline{\mathrm{qS1}(t)})(\mathrm{qS2}(t) - \overline{\mathrm{qS2}(t)}) \\ \sum_{i=1}^{N}(\mathrm{qS1}(t) - \overline{\mathrm{qS1}(t)})(\mathrm{qS2}(t) - \overline{\mathrm{qS2}(t)}) & \sum_{i=1}^{N}(\mathrm{qS2}(t) - \overline{\mathrm{qS2}(t)})^2 \end{bmatrix}, \tag{9}$$

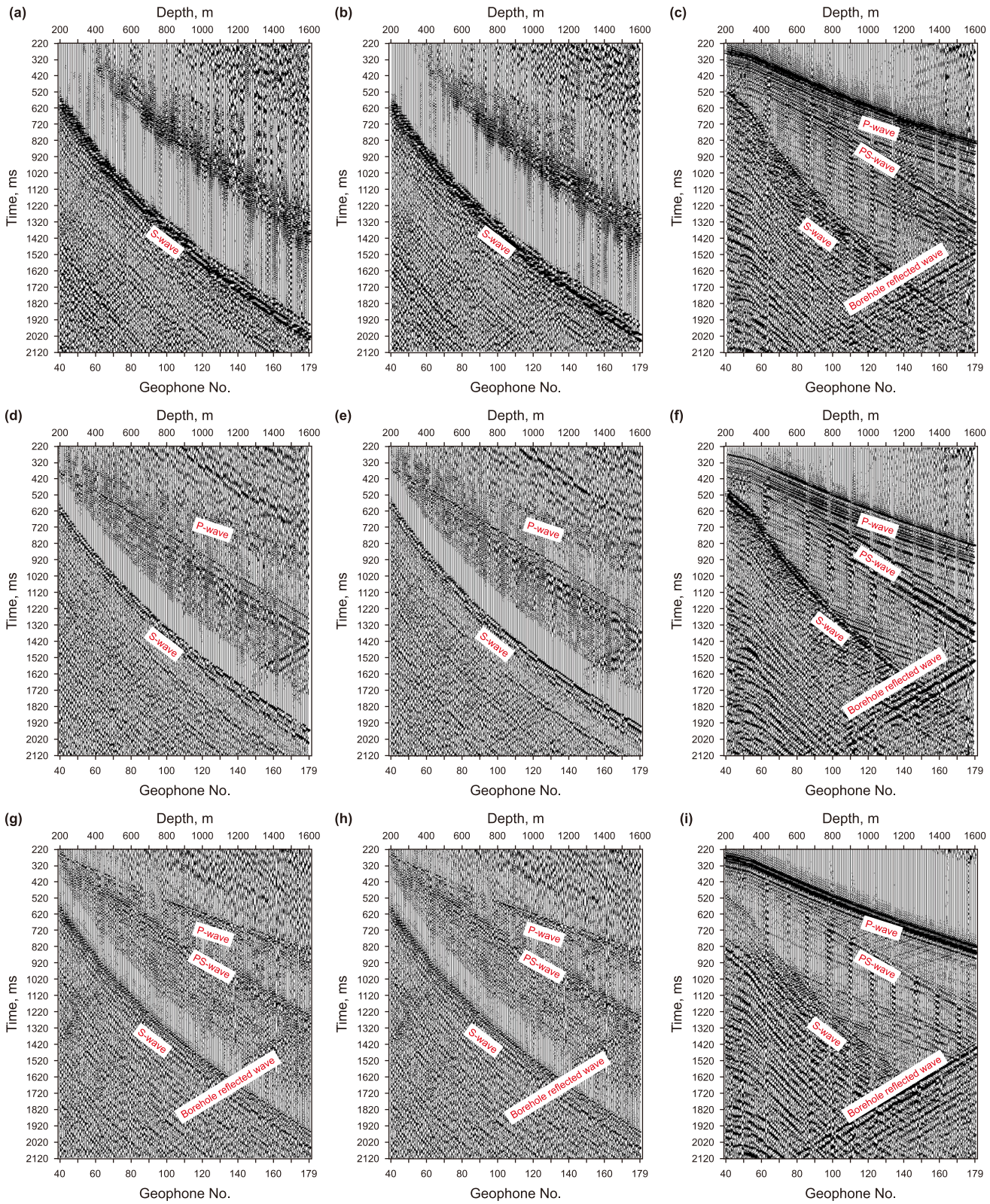

Fig. 3. The original nine-component VSP data: **(a)** *Xx*-component, **(b)** *Xy*-component, **(c)** *Xz*-component, **(d)** *Yx*-component, **(e)** *Yy*-component, **(f)** *Yz*-component, **(g)** *Zx*-component, **(h)** *Zy*-component, and **(i)** *Zz*-component.

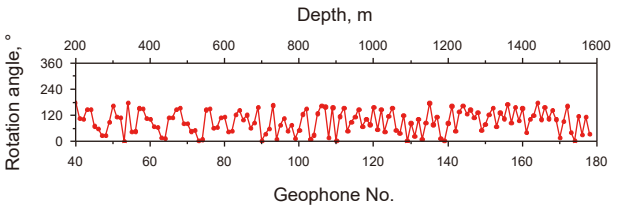

Fig. 4. Orientation deviations of the horizontal geophones.

where **D** presents the covariance matrix of the qS1(t) and qS2(t), and Δt is the time delay between the fast and slow shear waves, $\overline{\text{qS1}(t)}$ and $\overline{\text{qS2}(t)}$ are the average values of qS1(t) and qS2(t), separately.

The LTT is applied to the orientation-corrected downgoing four-component records. The SWS attributes are then calculated (Fig. 7). However, due to the fluctuation in the data points, predicting the fractured layers directly from the SWS attributes is challenging (the black points shown in Fig. 7(b) and (c)). To

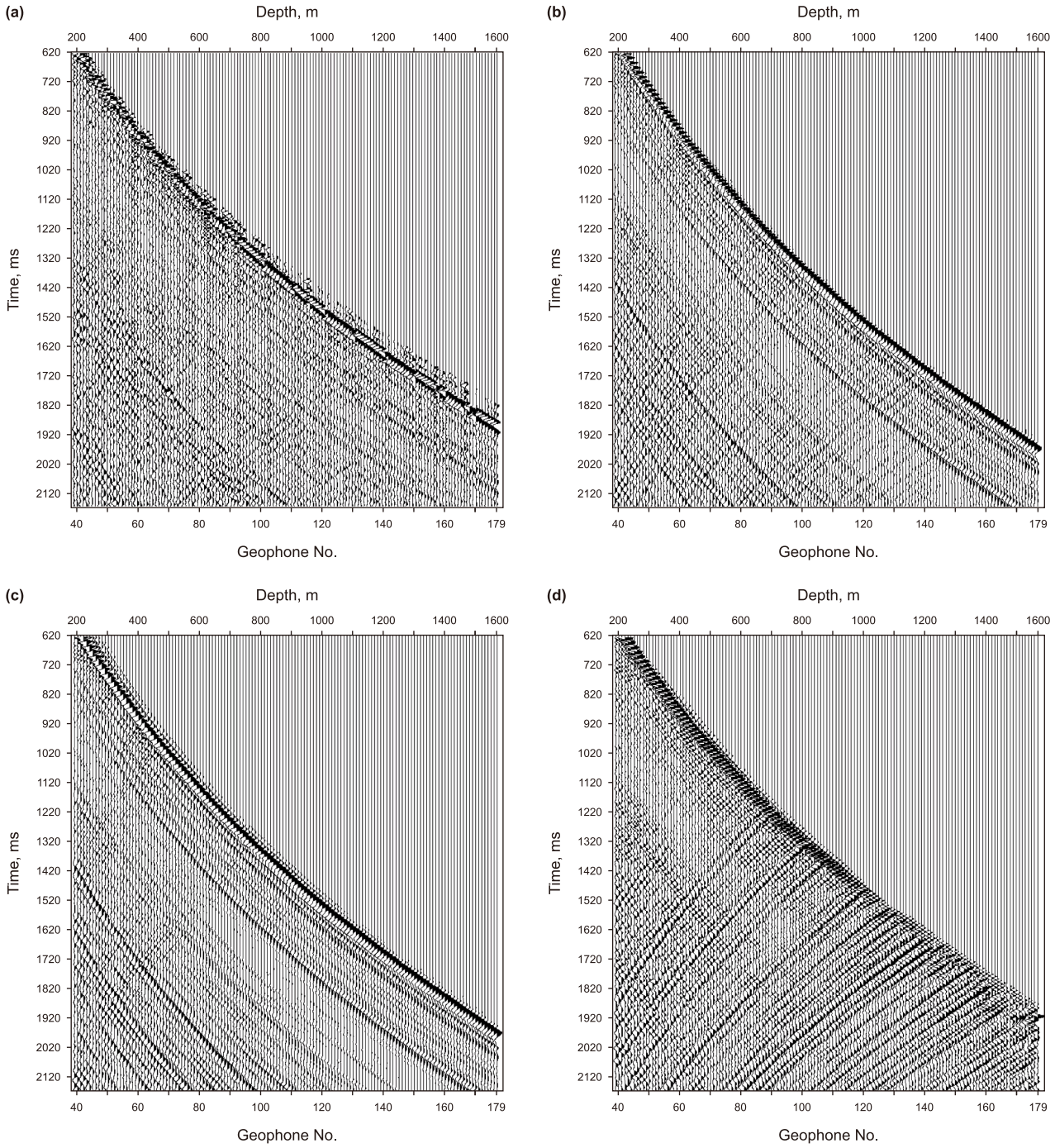

Fig. 5. The *Xx*-component **(a)** before and **(b)** after orientation correction. Separated **(c)** down-going and **(d)** up-going wavefields after FK filtering.

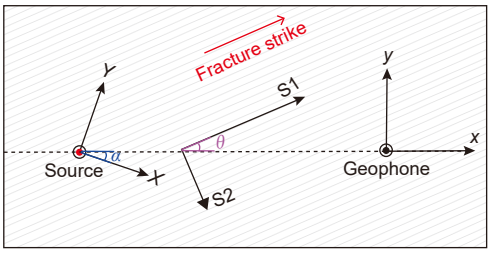

Fig. 6. Top view of the source coordinate (X, Y), receiver coordinate (x, y), and nature fracture geometry (S1, S2).

address this, a logistic function is used to fit the estimated SWS attributes, which can be expressed as (Reed and Berkson, 2002)

$$Y' = A_2 + \frac{A_1 - A_2}{1 + e^{-p(\ln X' - \ln X_0')}}, \tag{10}$$

where Y' represents the value of polarization or time delay, X' is the geophone index, and A_1, A_2, p, and X_0' are the parameters to be estimated. A_1 and A_2 represent the trend values of Y' within different geophone ranges. p is the slope of the transition of Y' from A_1 to A_2, and X_0' is the geophone position where Y' transitions from A_1 to A_2. To improve convergence efficiency and ensure the stability of the fitting process, we select the initial values of A_1 and A_2 as the maximum and minimum values of the observed Y', respectively. This strategy is based on the observation that logistic functions asymptotically approach these extremes. Field data validation shows that this approach reduces the number of required iterations by 40% compared to randomized initialization. For the initial value of the slope-related parameter p, it is typically set to 3, which corresponds to the average steepness observed in our data. This setting helps to approximate the general gradient trend of the data and mitigates the risks of divergence or poor local minima caused by an overly steep or flat initial slope. The parameters A_1, A_2, p, and X_0' are estimated using the least squares method, minimizing the error between the fitted curve and the actual data (Zhang, 2019).

The logistically fitted results are shown in Fig. 7(b) and (c) (red solid lines). There are two distinct SWS features from shallow to deep (indicated by ① and ②). The logistic-fitted polarization of the shallow section (geophone numbers from 40 to 120, as indicated in ①) is around 50°, and the corresponding time delay is around 13 ms. For the deeper section (geophone No. from 120 to 180 as indicated in ②), the polarization increases to 54°, while the time delay decreases to 12 ms. This phenomenon indicates the existence of two distinct fractured layers. The top of the shallow fractured layer is located at a depth above 200 m, while the top of the deep fractured layer is located at approximately 1000 m.

4. Quantitative interpretation of two fractured layers using a rock-physics-based method

The SWS analysis of the four-component VSP data reveals the presence of two fractured layers. Characterizing multiple fractured layers remains challenging; to address this issue, we propose a rock-physics-based method to invert the fracture parameters of each layer. The workflow is shown in Fig. 8.

4.1. Constructing the geological model and identifying two fractured layers

Before estimating the fracture parameters of the two layers, it is essential to identify their thicknesses. Gamma-ray index (GR) and acoustic impedance (AI) logs are employed for geological stratification, in which the GR log is used to delineate formations by distinguishing lithology variation, and the AI log is used to identify impedance contrasts corresponding to potential formation boundaries. Through the joint analysis of these well logs, we

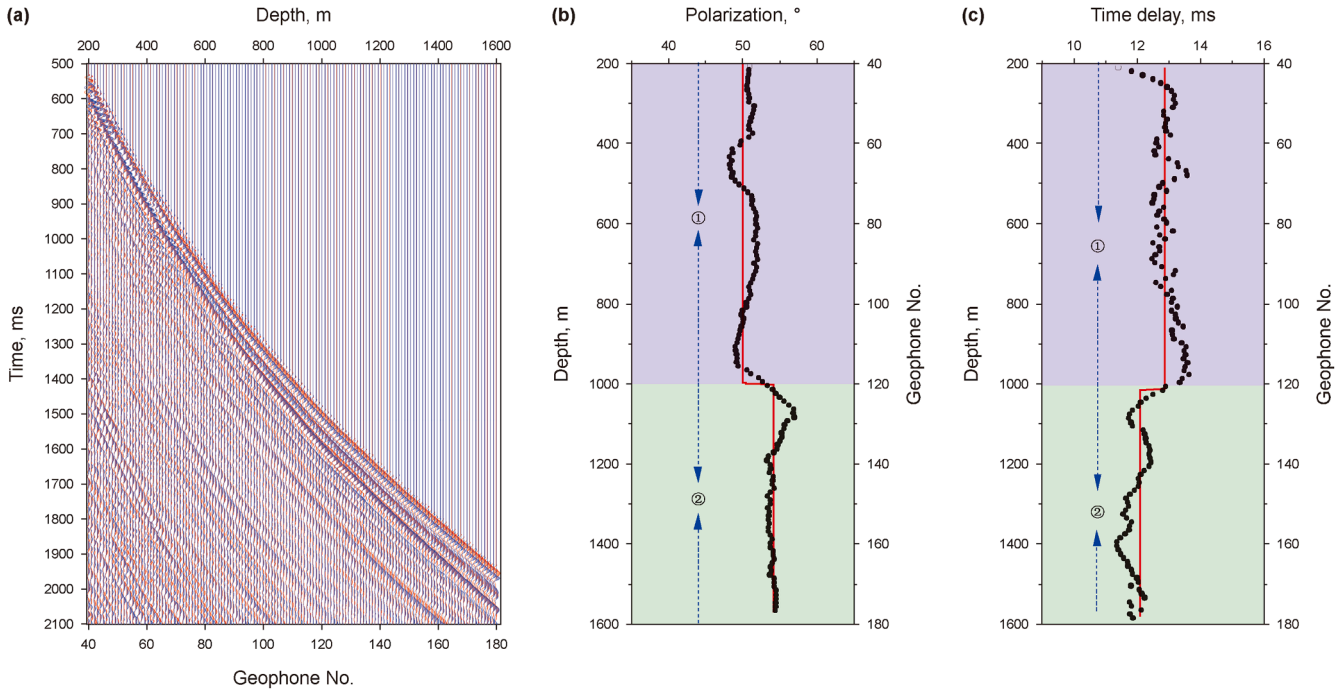

Fig. 7. **(a)** Seismic records of fast and slow shear waves from the field VSP, with red and blue representing the fast and slow shear waves, respectively. **(b)** The polarization of the fast shear wave and **(c)** the time delay between the fast and slow shear waves. The black point represents SWS attributes from the field VSP, while the solid red line represents the logistic fitting results.

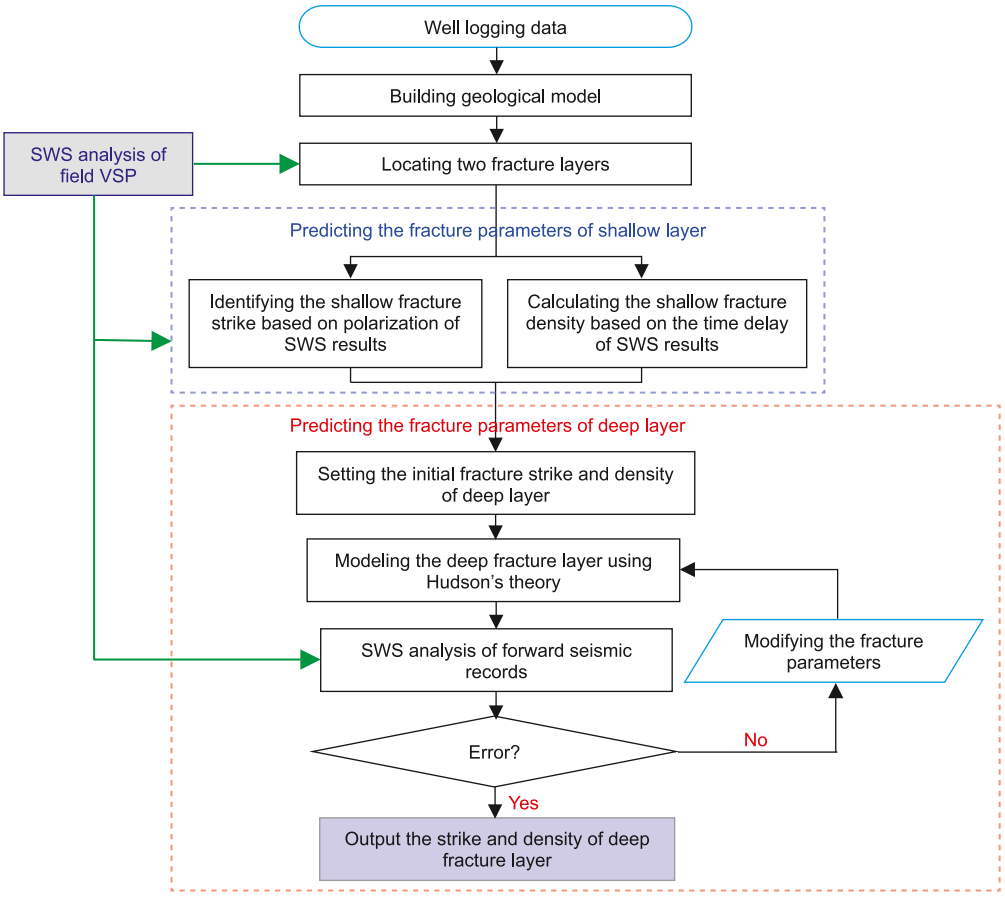

Fig. 8. Workflow for the quantitative interpretation of two fractured layers.

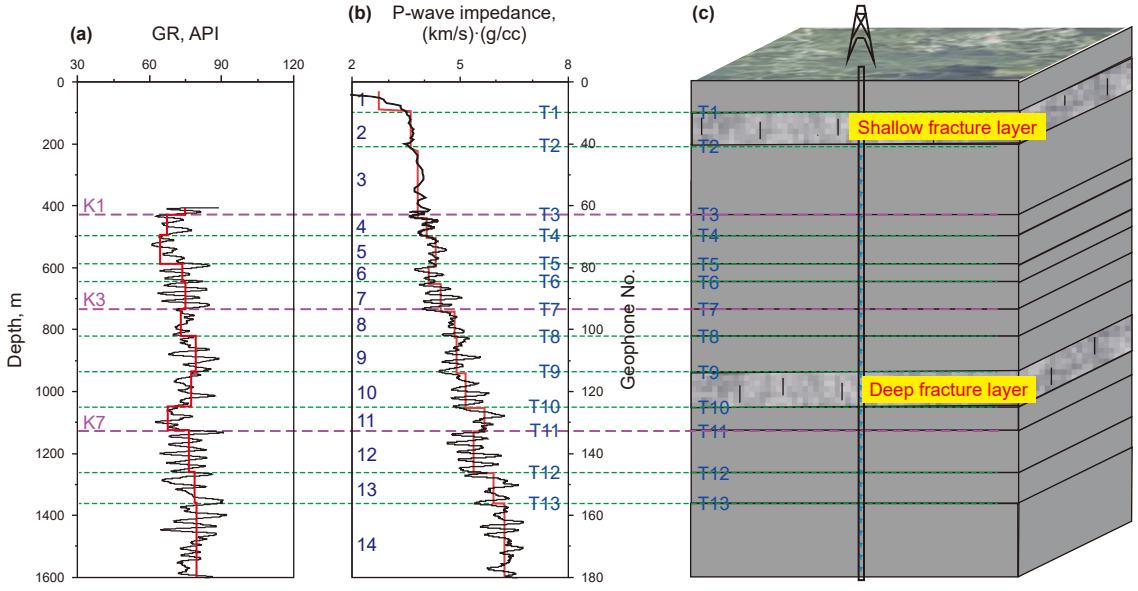

Fig. 9. Well log data of **(a)** gamma-ray index (GR) and **(b)** acoustic impedance (AI). **(c)** Interpreted geological model.

delineate 14 geological layers bounded by 13 interfaces, reflecting consistent lithological changes and acoustic contrasts (Fig. 9(a) and (b)). To validate the reliability of this stratification, we project interpreted seismic horizons from an adjacent well (e.g., K1, K3, and K7) onto the well shown in Fig. 9. The projected layer boundaries exhibit good agreement with the log-derived stratigraphy, supporting the consistency of the 14-layer division. The analysis of SWS attributes indicates that SWS occurs above a depth of 200 m and near 1000 m, corresponding to layers 2 and 10, respectively. Consequently, the shallow fractured layer is

identified between reflections T1 and T2, with a thickness of 105 m, while the deep fractured layer is located between reflections T9 and T10, with a thickness of 90 m. The resulting geological model is constructed accordingly, as shown in Fig. 9(c).

4.2. Interpretation of fracture parameters for the shallow fractured layer

SWS attributes enable direct quantification of fracture parameters. Based on the traditional data-driven method, the strike of the shallow fractures is directly related to the polarization of the fast shear wave, and the density of shallow fractures can be obtained using a rock-physics empirical relationship between the time delay and the fracture density. The empirical formula is expressed as follows (Schoenberg, 1988):

$$\frac{3(3-2r_b)}{3(3-2r_b)-16e}-1=\frac{\Delta t}{t_{S2}}, \tag{11}$$

where $r_b = (V_{S0}/V_{P0})^2$, and V_{S0} and V_{P0} are the vertical P-wave velocity and vertical S-wave velocity of the shallow fractured layer, respectively. Δt is the time delay between fast and slow shear waves, and t_{S2} is the traveltime of the slow shear wave, which can be obtained from the first arrival of slow shear wave records, and e denotes the fracture density. The values of V_{S0} and V_{P0} obtained from the VSP first arrivals are 657 m/s and 1723 m/s, t_{S2} is 154 ms, and the initial fracture density calculated using Eq. (12) is approximately 0.04.

The accuracy of the shallow fracture parameters is critical for the reliable estimation of deep fracture parameters. A rock-physics-based method is proposed to evaluate the accuracy of the estimated shallow fracture parameters. Firstly, the shallow fractured layer is modeled using Hudson's theory due to its mathematical simplicity, clear physical interpretation, and suitability for low-fracture-density conditions (fracture density < 0.1) (Hudson, 1981). The effective elastic coefficient ($\mathbf{C}^{\mathrm{eff}}$) of a shallow fractured layer can be expressed as follows:

$$\mathbf{C}^{\mathrm{eff}}=\mathbf{C}^{\mathrm{iso}}+\mathbf{C}^{\mathrm{ani}}. \tag{12}$$

$\mathbf{C}^{\mathrm{iso}}$ represents the elastic modulus of the isotropic background medium, and the form is

$$\mathbf{C}^{\mathrm{iso}}=\begin{bmatrix}\lambda+2\mu & \lambda & \lambda & 0 & 0 & 0\\ \lambda & \lambda+2\mu & \lambda & 0 & 0 & 0\\ \lambda & \lambda & \lambda+2\mu & 0 & 0 & 0\\ 0 & 0 & 0 & \mu & 0 & 0\\ 0 & 0 & 0 & 0 & \mu & 0\\ 0 & 0 & 0 & 0 & 0 & \mu\end{bmatrix}, \tag{13}$$

where λ and μ are the Lamé parameters of the isotropic medium. $\mathbf{C}^{\mathrm{ani}}$ represents the correction term caused by fracture. If only the first-order correction is considered, $\mathbf{C}^{\mathrm{ani}}$ is expressed as

$$\mathbf{C}^{\mathrm{ani}}=-\frac{e}{\mu}\begin{bmatrix}(\lambda+2\mu)^2U_{33} & \lambda(\lambda+2\mu)U_{33} & \lambda(\lambda+2\mu)U_{33} & 0 & 0 & 0\\ \lambda(\lambda+2\mu)U_{33} & \lambda^2U_{33} & \lambda^2U_{33} & 0 & 0 & 0\\ \lambda(\lambda+2\mu)U_{33} & \lambda^2U_{33} & \lambda^2U_{33} & 0 & 0 & 0\\ 0 & 0 & 0 & 0 & 0 & 0\\ 0 & 0 & 0 & 0 & \lambda^2U_{11} & 0\\ 0 & 0 & 0 & 0 & 0 & \lambda^2U_{11}\end{bmatrix}, \tag{14}$$

where e is the fracture density. U_{11} and U_{33} are the elastic parameters related to fracture characteristics.

$$U_{11}=\frac{16(\lambda+2\mu)}{3(3\lambda+4\mu)}\frac{1}{1+M}, \tag{15}$$

and

$$U_{33}=\frac{4(\lambda+2\mu)}{3(\lambda+\mu)}\frac{1}{1+k}, \tag{16}$$

where M and k are parameters related to the fracture characteristics, and they are expressed as follows:

$$M=\frac{4\mu'(\lambda+2\mu)}{\pi\mu(\lambda+\mu)}, \tag{17}$$

and

$$k=\frac{[K'+(4/3)\mu'](\lambda+2\mu)}{\pi\chi\mu(\lambda+\mu)}, \tag{18}$$

where K' and μ' are the bulk modulus and shear modulus of the filling in the fractures, respectively. χ is the aspect ratio (ASP ratio) of the fractures. The elastic and fracture parameters of the shallow fractured layer are listed in Table 1.

Then, the effective elastic coefficients calculated by Hudson's theory is

$$\mathbf{C}^{\mathrm{eff}}=\begin{bmatrix}4.9941 & 4.0912 & 3.8981 & 0 & 0 & 0\\ 4.0912 & 4.9941 & 3.8981 & 0 & 0 & 0\\ 3.8981 & 3.8981 & 4.5811 & 0 & 0 & 0\\ 0 & 0 & 0 & 0.4165 & 0 & 0\\ 0 & 0 & 0 & 0 & 0.4165 & 0\\ 0 & 0 & 0 & 0 & 0 & 0.4489\end{bmatrix}. \tag{19}$$

Based on the calculated effective elastic parameters of the shallow fractured layer, the four-component VSP seismic records of the shallow fractured layer are subsequently simulated using the reflectivity method (Fuchs and Müller, 1971). The acquisition geometry of the forward model is consistent with that of the field VSP. Using the forward seismic records, SWS analysis is performed using the LTT. Fig. 10 shows the comparison of fast and slow shear wave seismic records between the forward model and the field VSP. It can be seen that when geophone No. < 120, the first arrivals of the forward model are highly fitted with those of the field VSP (Fig. 10(a) and (c)), while when geophone No. > 120, there is a noticeable deviation between the first arrivals of the model and those of the field VSP (Fig. 10(b) and (d)). Fig. 11 shows the comparison of SWS attributes between the model and the field VSP at each geophone. The modeled polarization and time delay closely align with the SWS observations from the field VSP in the shallow section but deviate from those in the deep section.

4.3. Interpretation of fracture parameters for the deep fractured layer

The SWS attributes (50°, 13 ms) for the shallow fractured layer are illustrated by ① and the black solid circle in Fig. 12. The estimated shallow fracture parameters are a strike of 50° and a fracture density of 0.04, respectively. For the deep fractured layer, the

Table 1
The elastic parameters and fracture parameters of shallow fractured layer.

V_{P0}, km/s	V_{S0}, km/s	ρ, g/cc	Radius, m	ASP ratio (χ)	Fracture density (e)
1.7	0.66	2.12	1	0.001	0.04

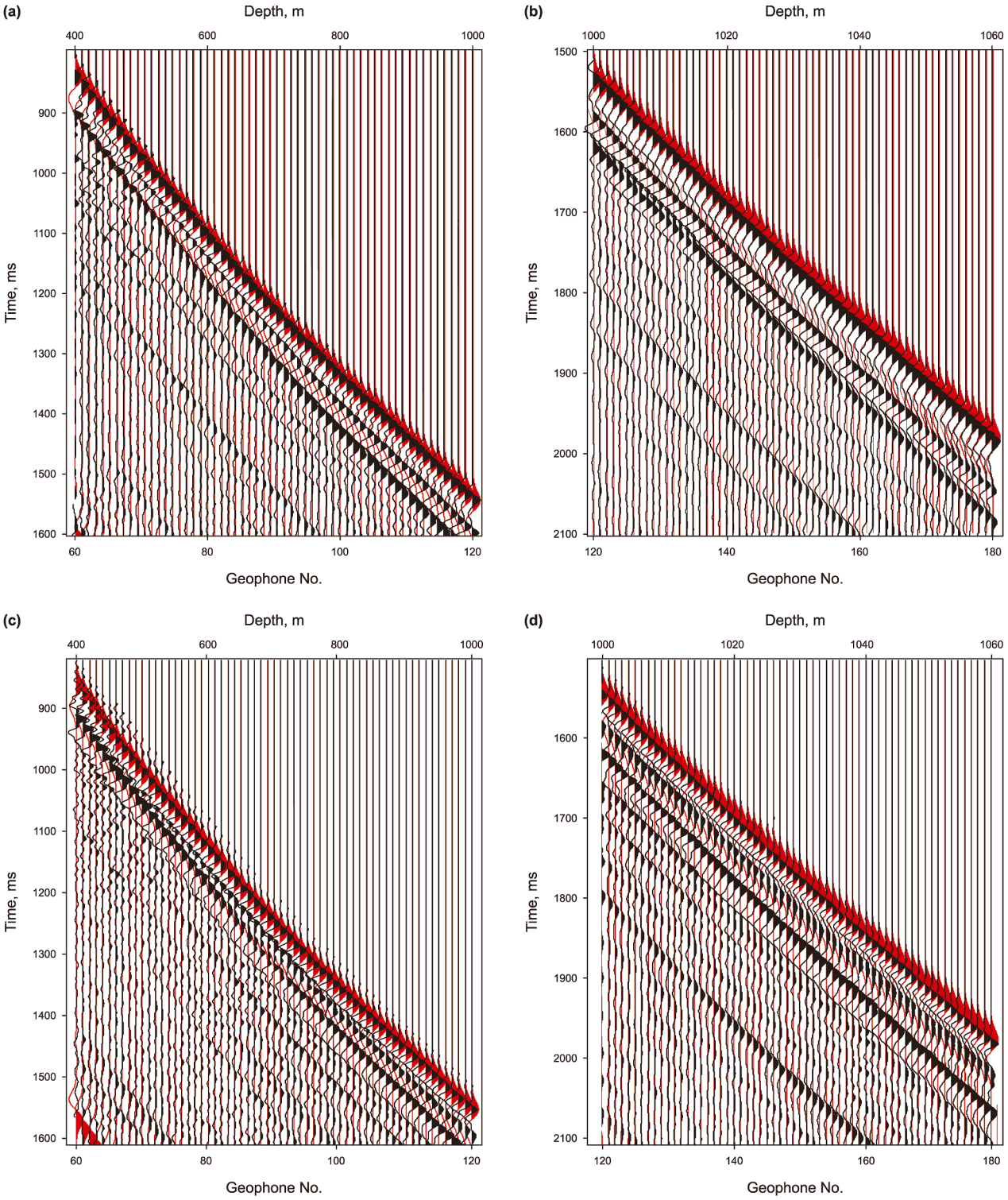

Fig. 10. Comparison of seismic records between the forward model and field VSP. **(a)** Fast shear wave for geophone No. < 120, and **(b)** fast shear wave for geophone No. > 120; **(c)** slow shear wave for geophone No. < 120, and **(d)** slow shear wave for geophone No. > 120. The red seismic records represent the forward model, while the black seismic records correspond to the field VSP.

SWS attributes derived from the field VSP are 54° and 12 ms, respectively, as illustrated by ② and the red star in Fig. 12. Using the traditional data-driven method, the estimated fracture strike and density are 54° and 0.037 for the deep layer. Incorporating both the shallow fracture parameters (50° and 0.04) and the deep fracture parameters (54° and 0.037), forward seismic records are modeled using the proposed method. The analyzed SWS attributes from the forward seismic records are 52° and 16.7 ms, respectively (illustrated by ②' and the black star in Fig. 12). A significant deviation is observed between ② and ②', highlighting that the deep

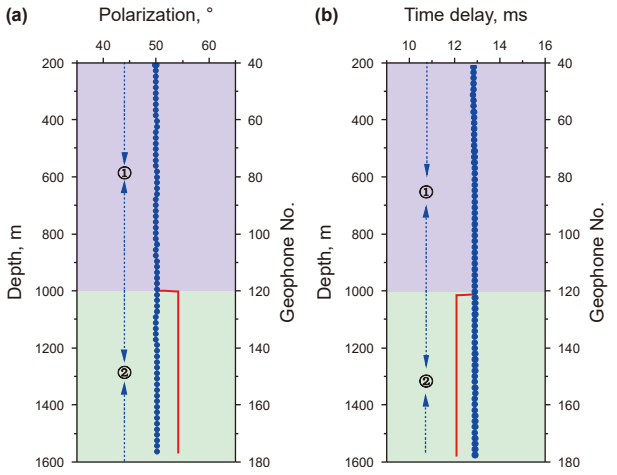

Fig. 11. **(a)** The polarization of the fast shear wave and **(b)** the time delay between the fast and slow shear waves. The solid red line represents SWS attributes derived from the field VSP, while the blue points correspond to those from the forward model.

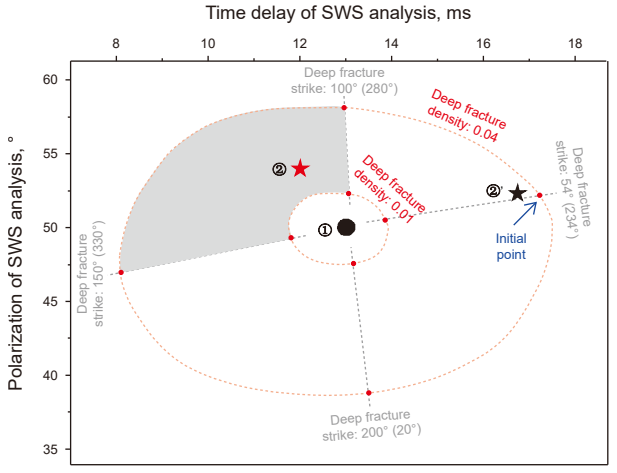

Fig. 12. The changes of SWS attributes induced by deep fracture parameters. ① represents the SWS attributes from field VSP corresponding to the shallow fractured layer, ② represents the SWS attributes from field VSP corresponding to the deep fractured layer, and ②' represents the SWS attributes from the model corresponding to the deep fracture parameters (54°, 0.037), considering the influence of shallow fracture parameters. The red solid circles represent the SWS attributes from forward models corresponding to the scanning deep fracture parameters. The red broken line is the contour of fracture density, and the black broken line is the contour of fracture strike.

fracture parameters directly estimated from the field SWS attributes fail to accurately reflect the true properties of the deep fractures due to the influence of the shallow fracture layer.

To improve computational efficiency and ensure the reliable estimation of deep fracture parameters, we adopted a hierarchical search strategy combining coarse- and fine-scale searches. A coarse-scale search is first conducted to determine the approximate range of the deep fracture parameters. The initial values are guided by shallow fracture parameters (e.g., fracture strike = 54° and density = 0.04). The fracture strike is searched over the full 0°–360°, and the fracture density is searched over a broad interval of 0–0.1. Given these fracture parameters, the synthetic seismic records are forward modeled, and the analyzed SWS attributes are illustrated by red dashed lines in Fig. 12. A highly non-monotonic relationship is observed between the fracture strike and the SWS attributes of the modeled seismic records. For a

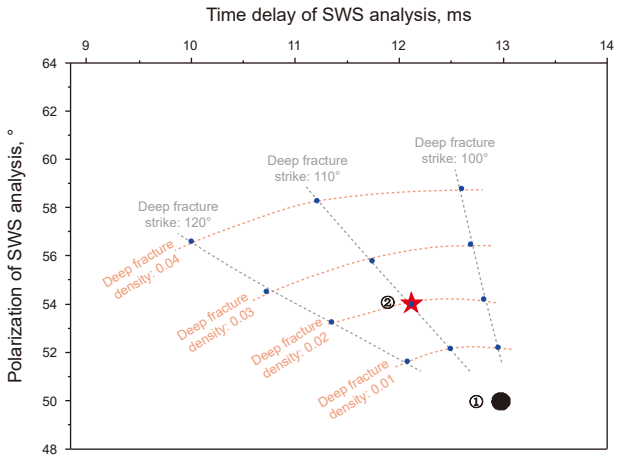

Fig. 13. The changes of SWS attributes induced by deep fracture parameters. ① represents the SWS attributes from field VSP corresponding to the shallow fractured layer, and ② represents the SWS attributes from field VSP corresponding to the deep fractured layer. The blue solid circles represent the SWS attributes from forward models corresponding to the scanning deep fracture parameters. The red broken line is the contour of fracture density, and the black broken line is the contour of fracture strike.

fixed fracture density (e.g., 0.04), as the deep fracture strike increases from 54° through a full rotation, the polarization angle initially increases, then decreases, and subsequently increases again, while the time delay initially decreases and then increases, forming a near-circular trajectory. Additionally, larger deep fracture densities cause the SWS attributes to deviate more significantly from those of the shallow fractured layer as represented by ① in Fig. 12. This coarse-scale search reveals that the deep SWS attributes from the field VSP (as indicated by ② in Fig. 12) correspond to the fracture parameters within a fracture strike range of 100°–150° and a fracture density range of 0.01–0.04 (gray area in Fig. 12).

Once an approximate solution is determined, a fine-scale search is performed within a narrow window (e.g., fracture strike: 100°–120°, fracture density: 0.01–0.04, as shown in Fig. 13), with scan intervals of 10° and 0.01, respectively. Within this refined range, a quantitative mapping between deep fracture parameters and SWS attributes is established through forward modeling. As shown in Fig. 13, the relationship between modeled SWS attributes and fracture parameters becomes monotonic, thereby facilitating more robust parameter estimation. The forward-modeled SWS attributes corresponding to fracture parameters of 110° for fracture strike and 0.02 for fracture density match those from the field VSP data. Fig. 14 shows that the predicted SWS parameters from this result exhibit strong agreement with the field VSP data. Notably, the traditional data-driven method overestimates the deep-layer fracture density, reaching nearly twice the value derived from our method (0.037 vs. 0.02), demonstrating that it may introduce substantial errors in complex multi-layered fracture systems (see Fig. 15).

Following the above analysis, we provide a quantitative interpretation of the two fractured layers in the study area (Fig. 16). The shallow fractured layer is characterized by a thickness of 105 m, a strike of 50°, and a density of 0.04. The deep fractured layer has a thickness of 90 m, a strike of 110°, and a density of 0.02.

5. Discussion

In this paper, the proposed method is demonstrated for a formation with two fractured layers. In practical applications, it can

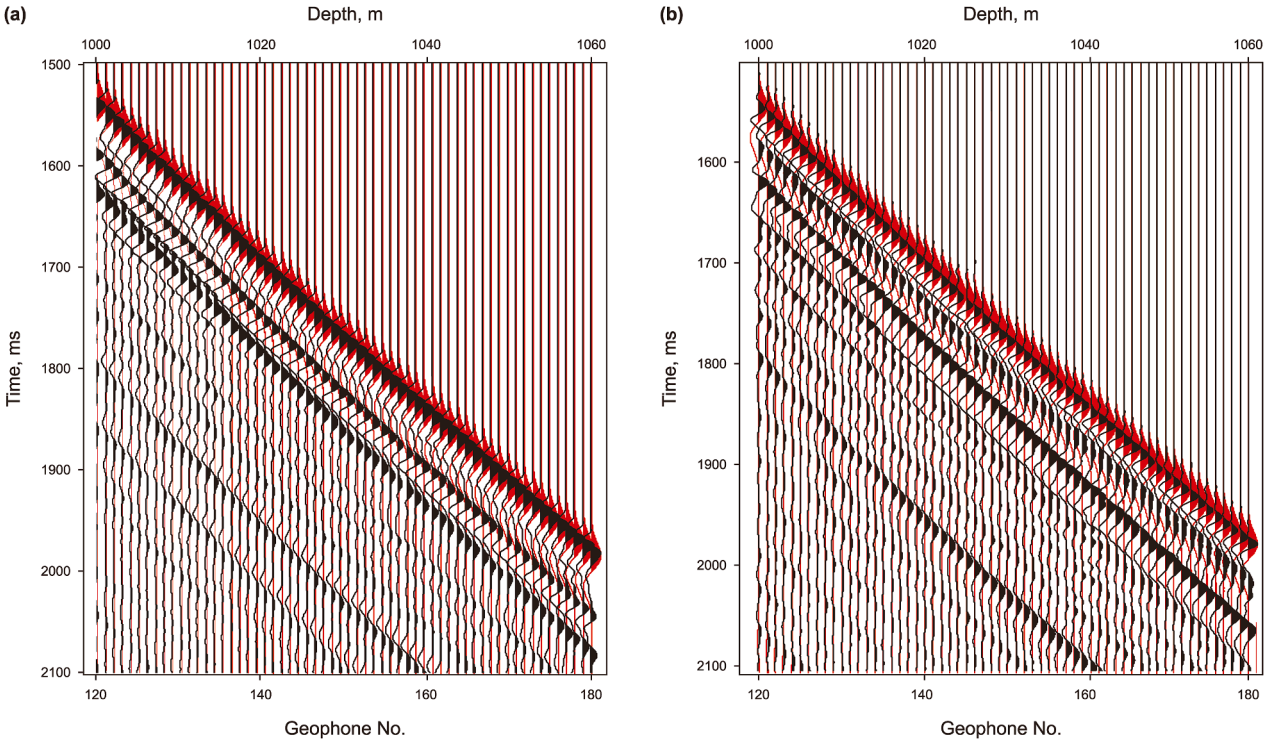

Fig. 14. Comparison of seismic records between the forward model and field VSP. **(a)** Fast shear wave for geophone No. > 120, and **(b)** slow shear wave for geophone No. > 120. The red seismic records represent the forward model, while the black seismic records correspond to the field VSP.

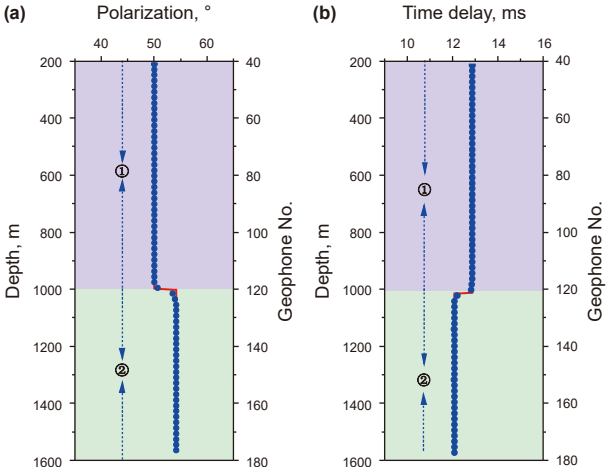

Fig. 15. **(a)** The polarization of the fast shear wave and **(b)** the time delay between the fast and slow shear waves. The solid red line represents SWS attributes derived from the field VSP, while the blue points correspond to those from the forward model.

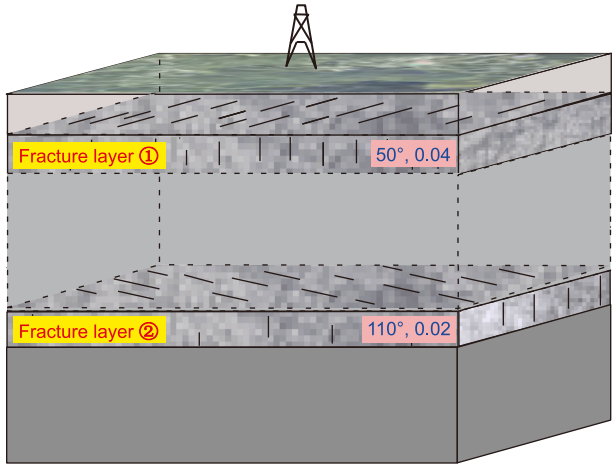

Fig. 16. Schematic diagram of the 3D model for fracture interpretation in the VSP area.

be extended to characterize multiple fractured layers. The inversion strategy can be applied sequentially from shallow to deep fractured layers.

Through rock physics modeling and forward modeling analysis, we demonstrate that deep fracture parameters cannot be directly calculated from SWS parameters when under the influence of a shallow fractured layer (Fig. 11). This study quantitatively analyzes the SWS response of deep fracture parameters to the influence of the shallow fractured layer, revealing that the influence of the shallow fractured layer on the behavior of the deep fractured layer presents a complex nonlinear relationship (Fig. 13).

6. Conclusion

In this paper, we characterize the development of subsurface structures in the VSP area located in the Sanhu Depression of the Qaidam Basin, China, using four-component shear wave VSP data. First, the VSP data are processed to obtain a high-quality downgoing wavefield, which is subsequently used for SWS analysis. The results show that there are two distinct SWS attributes from shallow to deep, which indicates the presence of two fractured layers. Characterizing multiple fractured layers, however, presents significant challenges due to the substantial influence of shallow fractured layers on the SWS attributes of deep fractured layers. To overcome these challenges, we propose a rock-physics-based

method to accurately predict the fracture parameters of two layers. The results show that the shallow fractured layer develops with a thickness of 105 m, a strike of 50°, and a density of 0.04. The deep fractured layer develops with a thickness of 90 m, a strike of 110°, and a density of 0.02. This investigation presents a reliable approach for the quantitative prediction of multi-layer fracture parameters. Moreover, the interpreted fracture parameters provide deeper insights into the migration and accumulation patterns of biogas reservoirs in the study area, offering valuable guidance for future exploration and development.

CRediT authorship contribution statement

Yi-Bo Chai: Writing – original draft, Methodology, Data curation, Conceptualization. **Feng Zhang:** Writing – review & editing, Methodology, Funding acquisition, Data curation. **Tao Xu:** Writing – review & editing. **Zhen Zou:** Data curation. **Xiang-Yang Li:** Writing – review & editing, Methodology, Formal analysis.

Declaration of competing interest

We declare that there is no conflict of interests regarding the publication of this paper. All authors have read the manuscript and approved to submit to your journal. The current manuscript has not been sent elsewhere for evaluation or presentation.

Acknowledgements

This work was supported by National Natural Science Foundation of China (W2431028), the SINOPEC Fundamental Research Program (P24258), and the CNPC Investigations on fundamental experiments and advanced theoretical methods in geophysical prospecting applications (2022DQ0604-02).

References

Alford, R.M., 1986. Shear data in the presence of azimuthal anisotropy: Dilley, Texas. In: SEG Technical Program Expanded Abstracts 1986, pp. 476–479. https://doi.org/10.1190/1.1893036.

Bale, R., Gratacos, B., Mattocks, B., et al., 2009. Shear wave splitting applications for fracture analysis and improved imaging: some onshore examples. First Break 27 (9), 73–83. https://doi.org/10.13810/j.cnki.issn.1000-7210.2022.05.003.

Corrigan, D., Withers, R., Darnall, J., et al., 1996. Fracture mapping from azimuthal velocity analysis using 3D surface seismic data. In: SEG Technical Program Expanded Abstracts 1996, pp. 1834–1837. https://doi.org/10.1190/1.1826495.

Crampin, S., 1984. An introduction to wave propagation in anisotropic media. Geophys. J. Roy. Astron. Soc. 76 (1), 17–28. https://doi.org/10.1111/j.1365-246X.1984.tb05018.x.

Ding, P.B., Di, B.R., Wei, J.X., et al., 2015. Experimental research on the effects of crack density based on synthetic sandstones contain controlled fractures. Chin. J. Geophys. 58 (4), 1390–1399. https://doi.org/10.6038/cjg20150425 (in Chinese).

Donati, M., Piazza, J.L., Rollet, A., et al., 2016. 3D-3C multicomponent seismic – A successful fracture characterization case study in Algeria. First Break 34 (1), 31–43. https://doi.org/10.1190/segam2014-0835.1.

Fu, X., Cao, D., Zhang, F., 2025. Deep learning-based denoising of pre-stack seismic angle gathers with application to time-lapse data. Geophysics 91 (1), 1–82. https://doi.org/10.1190/geo2024-0472.1.

Fuchs, K., Gerhard, M., 1971. Computation of synthetic seismograms with the reflectivity method and comparison with observations. Geophys. J. Int. 23 (4), 417–433. https://doi.org/10.1111/j.1365-246X.1971.tb01834.x.

Garotta, R., Granger, P.Y., 1988. Acquisition and processing of 3C× 3-D data using converted waves. In: SEG Technical Program Expanded Abstracts 1988, pp. 995–997. https://doi.org/10.1190/1.1892469.

Gholami, R., Moradzadeh, A., Rasouli, V., et al., 2016. Shear wave splitting analysis to estimate fracture orientation and frequency dependent anisotropy. Acta Geophys 64 (1), 76–100. https://doi.org/10.1515/acgeo-2015-0060.

Gong, T., Wang, Z.L., Luo, W.S., et al., 2022. Four-component rotation and fast-slow wave separation techniques for 3D vector S-wave seismic data of S-wave sources. Oil Geophys. Prospect. 57 (5), 1028–1034. https://doi.org/10.13810/j.cnki.issn.1000-7210.2022.05.003.

Greenhalgh, S.A., Mason, I.M., 1995. Orientation of a downhole triaxial geophone. Geophysics 60 (4), 1234–1237. https://doi.org/10.1190/1.1443852.

Guo, G.H., Shi, S.H., Yan, H.J., et al., 2008. Azimuth-dependence of shear-wave splitting in EDA media. Two-dimensional three-component pseudo-spectral modeling. Chin. J. Geophys. 51 (2), 469–478 (in Chinese).

Heggland, R., 1997. Detection of gas migration from a deep source by the use of exploration 3D seismic data. Mar. Geol. 137 (1-2), 41–47. https://doi.org/10.1016/S0025-3227(96)00077-1.

Huang, D.F., 2010. Cenozoic Sedimentation and Structure of Tainan 9 Well Area in Sanhu Depression, Qaidam Basin. M.S. thesis, China University of Petroleum, East China.

Hudson, J.A., 1981. Wave speeds and attenuation of elastic waves in material containing cracks. Geophys. J. Int. 64 (1), 133–150. https://doi.org/10.1111/j.1365-246X.1981.tb02662.x.

Kang, N.C., Jiao, G.H., Cai, J.M., 2009. Oil geologic feature in Sanhu depression of Qaidam Basin and next exploration and study direction. Oil Geophys. Prospect. 44 (4), 508–514. https://doi.org/10.13810/j.cnki.issn.1000-7210.2009.04.008.

Li, X.Y., Wang, Y., Sun, P.Y., et al., 2024. Shear-wave splitting and P-wave azimuthal anisotropy in oil and gas exploration seismic. Chin. J. Geophys. 67 (3), 855–870. https://doi.org/10.6038/cjg2023R0643 (in Chinese).

Li, A., Sun, D., Wang, H., et al., 2011. Seismic velocity and shear-wave splitting under cyclic loading. IEEE, pp. 4506–4508. https://doi.org/10.1109/ICECC.2011.6068054.

Li, L., Zhang, J.J., Pan, X.P., et al., 2020. Azimuthal elastic impedance-based Fourier coefficient variation with angle inversion for fracture weakness. Pet. Sci. 17 (1), 86–104. https://doi.org/10.1007/s12182-019-00405-0.

Li, M.Q., Stovas, A., Lu, J., et al., 2022. Inversion of fracture weaknesses based on linearly approximated traveltime. IEEE Trans. Geosci. Rem. Sens. 60, 5920913. https://doi.org/10.1109/TGRS.2022.3211081.

Li, X.Y., 1998. Processing PP and PS waves in multicomponent sea-floor data for azimuthal anisotropy: Theory and overview. Rev. Inst. Fr. Petrol 53 (5), 607–620. https://doi.org/10.2516/ogst:1998055.

Li, X.Y., Crampin, S., 1993. Linear-transform techniques for processing shear-wave anisotropy in four-component seismic data. Geophysics 58 (2), 240–256. https://doi.org/10.1190/1.1443409.

Liu, Z., Zhang, F., Li, X., 2019. Elastic anisotropy and its influencing factors in organic-rich marine shale of southern China. Sci. China Earth Sci. 62 (11), 1805–1818. https://doi.org/10.1007/s11430-019-9449-7.

Maultzsch, S., Chapman, M., Liu, E., et al., 2003. Modelling frequency-dependent seismic anisotropy in fluid-saturated rock with aligned fractures: Implication of fracture size estimation from anisotropic measurements. Geophys. Prospect. 51 (5), 381–392. https://doi.org/10.1046/j.1365-2478.2003.00386.x.

Mueller, M.C., 1991. Prediction of lateral variability in fracture intensity using multicomponent shear-wave surface seismic as a precursor to horizontal drilling in the Austin Chalk. Geophys. J. Int. 107 (3), 409–415. https://doi.org/10.1111/j.1365-246X.1991.tb01402.x.

Prajapati, S., Ghosh, D., 2015. Analysis of shear-wave splitting using multicomponent seismic data. In: SEG Technical Program Expanded Abstracts. Society of Exploration Geophysicists, Tulsa, pp. 377–382.

Reed, L.J., Joseph, B., 2002. The application of the logistic function to experimental data. J. Phys. Chem. 33 (5), 760–779.

Schoenberg, M., Douma, J., 1988. Elastic wave propagation in media with parallel fractures and aligned cracks1. Geophys. Prospect. 36 (6), 571–590. https://doi.org/10.1111/j.1365-2478.1988.tb02181.x.

Silver, P.G., Chan, W.W., 1991. Shear wave splitting and subcontinental mantle deformation. J. Geophys. Res. Solid Earth 96 (10), 16429–16454. https://doi.org/10.1029/91JB00899.

Sun, S.Z., Zhou, X., Yang, H., et al., 2011. Fractured reservoir modeling by discrete fracture network and seismic modeling in the Tarim Basin, China. Pet. Sci. 8 (4), 433–445. https://doi.org/10.1007/s12182-011-0161-x.

Thomsen, L., 1988. Reflection seismology over azimuthally anisotropic media. Geophysics 53 (3), 304–313. https://doi.org/10.1190/1.1442464.

Thomsen, L., Tsvankin, I., Mueller, M.C., 1999. Coarse-layer stripping of vertically variable azimuthal anisotropy from shear waves data. Geophysics 64 (4), 1126–1138. https://doi.org/10.1190/1.1444619.

Wang, X.C., Bai, W., Zheng, Y.P., 2020. Research on the anisotropy of gas hydrate reservoirs in South China Sea. Mar. Geophys. Res. 41 (4), 16. https://doi.org/10.1007/s11001-020-09415-9.

Wang, Y., Wang, C., Li, J., et al., 2019. Frequency-dependent S-wave splitting parameters analysis: A case study from azimuthal PS data, Sanhu area of the Qaidam Basin, China. Geophysics 84 (6), B375–B386. https://doi.org/10.1190/geo2018-0627.1.

Wu, C.Z., Zhang, F., Ding, P.B., et al., 2024. Rock-physics model of a gas hydrate reservoir with mixed occurrence states. Geophysics 89 (2), MR53–MR62. https://doi.org/10.1190/geo2023-0211.1.

Wu, C.Z., Han, L., Zhang, F., et al., 2023. Gas hydrate reservoir identification based on rock physics modelling and sensitive elastic parameters. J. Geophys. Eng. 20 (1), 117–127. https://doi.org/10.1093/jge/gxac100.

Xiao, W.D., Ding, W.N., Xu, T.J., et al., 2013. Fracture detection with layer-stripping of PS-wave splitting. Oil Geophys. Prospect. 48 (6), 966–971. https://doi.org/10.13810/j.cnki.issn.1000-7210.2013.06.017.

Yardley, G.S., Crampin, S., 1991. Extensive-dilatancy anisotropy: Relative information in VSPs and reflection surveys. Geophys. Prospect. 39 (3), 337–355. https://doi.org/10.1111/j.1365-2478.1991.tb00316.x.

Zhang, F., Zhang, T., Li, X.Y., 2019. Seismic amplitude inversion for the transversely isotropic media with vertical axis of symmetry. Geophys. Prospect. 67 (9), 2368–2385. https://doi.org/10.1111/1365-2478.12842.